CCFE
CULHAM CENTRE FOR FUSION ENERGY

UK Atomic Energy Authority

UKAEA-CCFE-CP(25)15

S. Henderson, M. Bernert, D. Brida, G. Derks, S. Elmore, J. Harrison, B. Kool, N. Lonigro, J. Lovell, D. Moulton, H. Reimerdes, P. Ryan, J. Stobbs, K. Verhaegh, T. Wijkamp

Validating reduced models for detachment onset and reattachment timescales

Validating reduced models for detachment onset and reattachment timescales

S. Henderson, M. Bernert, D. Brida, G. Derks, S. Elmore, J. Harrison, B. Kool, N. Lonigro, J. Lovell, D. Moulton, H. Reimerdes, P. Ryan, J. Stobbs, K. Verhaegh, T. Wijkamp

This paper has been submitted to
26th International Conference on Plasma Surface Interaction (PSI) in Controlled Fusion Devices, Marseille, France, 12 - 17 May 2024

Validating reduced models for detachment onset and reattachment times on MAST-U

S. S. Henderson[a], M. Bernert[b], D. Brida[b], G. L. Derks[d,e], S. Elmore[a], F. Federici[c], J. R. Harrison[a], A. Kirk[a], B. Kool[d,e], N. Lonigro[a,f], J. Lovell[c], D. Moulton[a], H. Reimerdes[g], P. Ryan[a], J. Stobbs[a], K. Verhaegh[a], T. V. D. Doel[d,e], T. Wijkamp[d], O. Bardsley[a], The MAST-U Team[h], The EUROfusion Tokamak Exploitation team[i]

[a] *United Kingdom Atomic Energy Authority, Culham Campus, Abingdon ,OX14 3DB, UK*
[b] *Max Plank Institute for Plasma Physics, Boltzmannstr. 2, Garching 85748, Germany*
[c] *Oak Ridge National Laboratory, Oak Ridge, TN, 37831, USA*
[d] *Dutch Institute for Fundamental Energy Research, Eindhoven, The Netherlands*
[e] *Eindhoven University of Technology, Control Systems Technology, Eindhoven, The Netherlands*
[f] *York Plasma Institute, University of York, York, UK*
[g] *EPFL, Swiss Plasma Centre (SPC), Lausanne CH-1015, Switzerland*
[h] *See the author list of J. Harrison et al 2019 Nucl. Fusion 59 112011*
[i] *See the author list of E. Joffrin et al 2024 Nucl. Fusion in press*
https://doi.org/10.1088/1741-4326/ad2be4

Abstract

Two reduced models are validated, which predict detachment onset and divertor reattachment times on MAST Upgrade (MAST-U). These models are essential for future tokamak reactor design, providing rapid calculations using primarily engineering parameters. The first model predicts detachment onset using a qualifier developed on ASDEX Upgrade (AUG) and later tested on JET, while the second model describes a static relation to estimate the time required for burn-through of neutral particles in the divertor for a given transient. Experiments were conducted on MAST-U in H-mode plasma scenarios with double-null and single-null configurations, involving D_2 fuelling ramps and N_2 seeding. The detachment onset was determined by monitoring divertor parameters such as the target heat flux profile, electron temperature, and electron density, with measurements showing consistency with AUG-derived predictions. The reattachment times were assessed during dynamic vertical shifts of the plasma centroid position, with observations indicating reattachment within milliseconds, consistent with model predictions. Overall, results confirm the applicability of both reduced models to MAST-U, extending their validation beyond AUG and JET.

Keywords: Detachment onset, Divertor reattachment, Impurity seeding, MAST Upgrade

1. Introduction

A major focus in fusion research is the design of future power plant reactors [1]. Low-fidelity (reduced) models often play a leading role in identifying possible operational points for fusion reactors due to their rapid calculation times [2]. Reduced models usually have the benefit of being tested over a broad domain, either because they are inherently built on multi-machine database regressions or because they can be more readily applied across larger datasets. Consequently, they can also serve as a coarse consistency check for high-fidelity simulations. Given the significant technological gap between current tokamak research experiments and future burning tokamaks, it is critical to continue the validation of reduced and high-fidelity models. This paper aims to further validate two reduced models for predicting detachment access and divertor reattachment burn-through times.

Divertor detachment is crucial for ensuring that future integrated reactor plasma scenarios are compatible with tolerable heat loads and levels of erosion within the divertor region [3]. Moreover, a divertor detachment control system is essential to manage transient events, such as fluctuations in power crossing the separatrix or towards the individual divertors, changes in density in the divertor region, or even failures in impurity gas or pellet injection systems [4, 5]. Predicting the time required to ionise, or 'burn-through', the volume of neutrals in front of the target plate during a given power transient is critical for establishing the allowable response time in the control system. The remaining challenge then lies in accurately predicting the timescales associated with various power transients and determining whether the steady-state detachment solution can be optimised to increase the burn-through time. Ideally, the burn-through becomes so large that the neutral volume never fully ionises over the transient timescale, allowing the expected transients to be absorbed passively.

Detachment access is predicted using a simple qualifier developed on ASDEX Upgrade (AUG) [6, 7]:

$$q_{\mathrm{det}} = 1.3 \frac{P_{\mathrm{sep}}/R_{\mathrm{maj}}\left(5\mathrm{mm}/\lambda_{\mathrm{int}}\right)}{p_0\left(1+f_Z c_Z\right)} \left(\frac{1.65\mathrm{m}}{R_{\mathrm{maj}}}\right)^{0.1}. \tag{1}$$

The parameters in the numerator of the first ratio arise due to the dependence on the parallel energy flux density, where P_{sep} is the power crossing

the separatrix, R_{maj} is the major radius, and λ_{int} is the power decay width including broadening. The denominator is associated with the power dissipation through momentum and radiation loss, where p_0 is the divertor neutral pressure, c_Z is an average scrape-off layer (SOL) impurity concentration, and f_Z is a factor describing the impurities ability to radiate relative to deuterium, e.g. for nitrogen $f_{\mathrm{N}} = 18$. The ratio in brackets appears due to the weak scaling with connection length. The factor 1.3 is chosen such that $q_{\mathrm{det}} = 1$ corresponds to partial detachment on AUG, defined as a significant reduction of heat flux and pressure along field lines between the midplane and divertor target within a power decay length in the SOL.

The time taken to burn-through the neutrals is described using a simple static relation developed on AUG [8]:

$$t^{\mathrm{B-T}} = 0.09\sqrt{\left(\frac{p_0}{2\mathrm{Pa}}\right)\left(\frac{n_{\mathrm{e}}}{3\times10^{20}\ \mathrm{m}^{-3}}\right)\left(\frac{V}{0.4\ \mathrm{m}^3}\right)\left(\frac{L_{\mathrm{X}}}{12\ \mathrm{m}}\right)\left(\frac{t^{\mathrm{max}}}{0.2\ \mathrm{s}}\right)\left(\frac{2.67\ \mathrm{MW}}{\Delta P}\right)}.$$

V is an estimate of the volume of neutrals in front of the target, L_{X} is the connection length between the X-point and target normalised by the value found in the flux surface ≈ 1 mm away from the separatrix on AUG, n_{e} is the electron density in the divertor region normalised by the average value determined by spectroscopic Stark broadening measurements, and t^{max} and ΔP denote the total duration and magnitude of the power transient, respectively. The formula is derived by assuming a linearly increasing power, $P(t) = t\Delta P/t^{\mathrm{max}}$, and a constant divertor neutral pressure during the power transient. The impact of these approximations, requires further understanding from both experiments and higher fidelity modelling.

Previous studies tested these two reduced models on AUG and JET, in single-null configuration with vertical-vertical inner-outer divertor geometry [6, 7, 8, 9]. The experiments assessed mixtures of N, Ne, and Ar impurity gases and applied both impurity gas cuts and step increases of the neutral beam injection power up to 5 MW during phases of deep detachment. The validation is now expanded to ELMy H-mode MAST-U plasma scenarios, which feature both single-null and double-null configuration with significantly different divertor geometry to both AUG and JET.

The structure of this paper is as follows: Section 2 presents a description of the MAST-U H-mode plasma scenario, incorporating fuelling ramps and N_2 seeding. This section also includes the validation of the detachment qualifier. Section 3 provides an overview of the power transients induced in the H-mode plasma scenario by variations in the vertical position of the

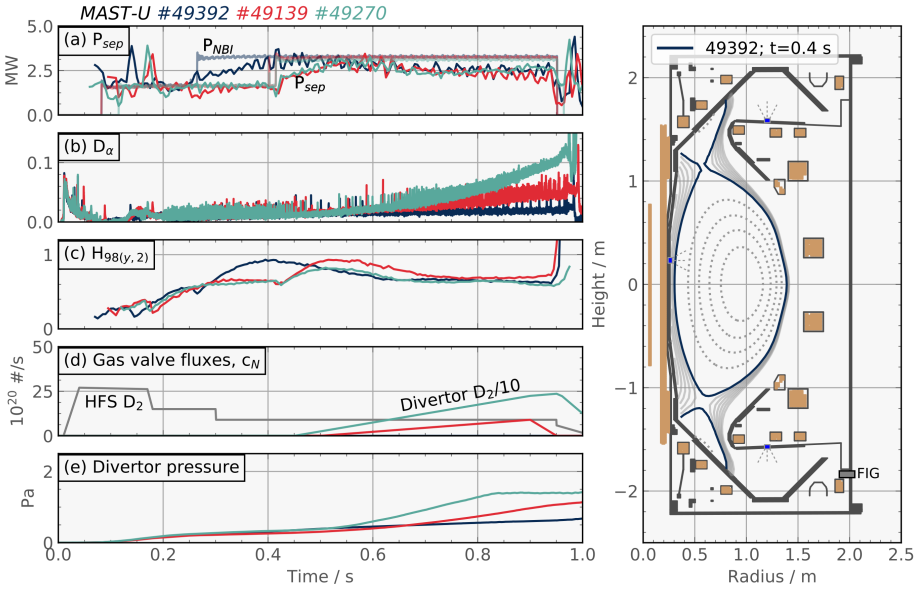

Figure 1: MAST-U fuelling ramp scans in H-mode for detachment onset determination.

plasma centroid, along with an assessment of the detachment front burn-through time. Finally, the conclusions are given in Section 4.

2. Assessment of detachment onset

The detachment onset is assessed on MAST-U in a double-null H-mode plasma with plasma current $I_\mathrm{P} = 0.75$ MA, toroidal field on axis $B_0 = 0.55$ T, neutral beam injection power $P_\mathrm{NBI} = 3.4$ MW, and major and minor radii $R_\mathrm{maj} = 1$ m and $a_\mathrm{min} = 0.55$ m, respectively. The plasma time traces and machine geometry are shown in Fig. 1. The magnetic configuration is setup with vertical-horizontal inner-outer divertor geometry and outer target strike-point in 'conventional' location (i.e., $R_\mathrm{t,outer} \approx R_\mathrm{maj}$). Regular ELMs are observed throughout the majority of the scenario; a reduction in the $\mathrm{H}_{98(y,2)}$ confinement factor is typical in most MAST-U H-mode scenarios to date due to MHD that slows down and locks [10]. A low level D_2 puff is applied through the high-field side midplane valve during the H-mode phase, resulting in a rising divertor pressure between $p_0 = 0.3 - 0.6$ Pa, as measured by the Fast Ion Gauge (FIG) located in the sub-divertor. The gas valve fluxes shown in Fig. 1 (and also later in 2) are requested flow rates and do not necessarily represent exactly the true injected flow rates.

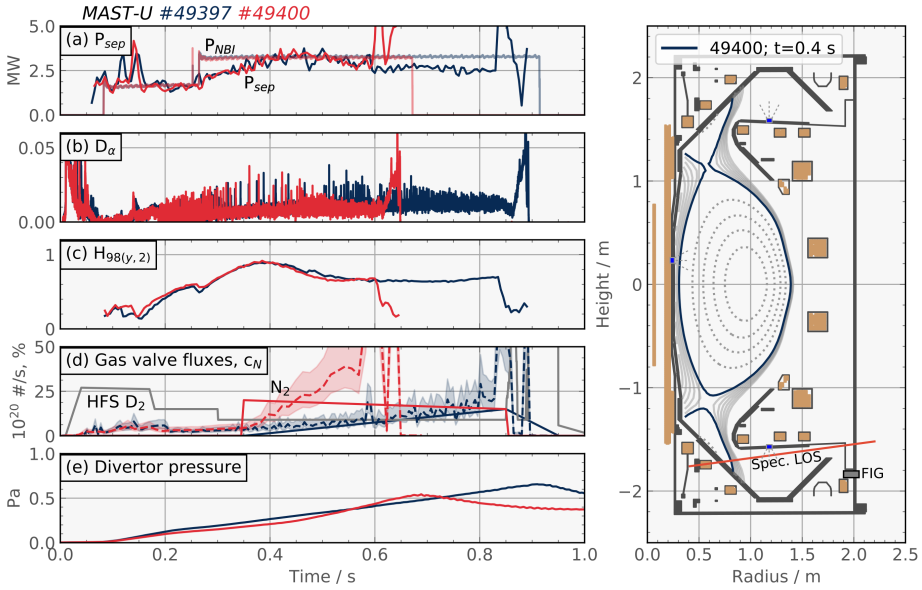

Figure 2: MAST-U N_2 seeding scans in H-mode for detachment onset determination.

To induce detachment, firstly the divertor pressure is raised by additional D_2 puffing through gas valves located within the upper and lower outer divertor chambers. The divertor pressure rises linearly with the applied D_2 puff up to a value of ≈ 1 Pa and > 1.45 Pa (FIG saturates at ≈ 1.45), respectively, in the two fuelling ramp scenarios shown. The midplane D_α emission also increases in line with the D_2 puff and indicates an increase in ELM frequency after the D_2 ramp begins. During this phase, the pedestal top temperature drops from ≈ 250 eV to ≈ 100 eV. A drop in peak $H_{98(y,2)}$ from ≈ 0.95 to ≈ 0.8 is found between the scenario with and without a fuelling ramp; however, $H_{98(y,2)}$ stabilises at $\approx 0.6 - 0.7$ in all scenarios.

Next, the D_2 puff was replaced by both a ramp and a flat level of N_2 seeding from the same valve locations. The plasma traces and equilibrium are shown in Fig. 2. It was necessary to move the outer strike-point ≈ 2 cm outwards in comparison to the D_2 scenario to help stabilise the scenario at higher N_2 seeding levels; however, at N_2 seeding rates of $\approx 2 \times 10^{21}$ atoms/s the MHD still locks causing the scenario to disrupt. The pedestal behaviour following the N_2 injection is similar to the D_2 fuelled scenario, showing a drop in pedestal temperature and an increase in ELM frequency. While the divertor pressure is rising during the seeding scenario, the injection of N_2 causes only a small change in pressure between the two scenarios.

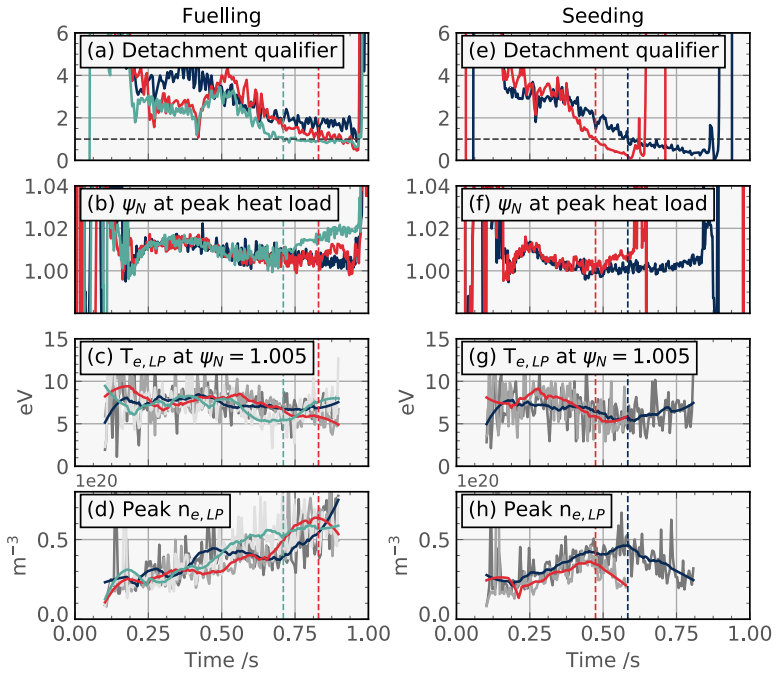

Figure 3: Overview of divertor measurements during fuelling and seeding scans of Fig. 1 and 2.

The divertor N concentration, c_{N}, is determined through visible spectroscopy using previously established methodology [11]. This method connects the N II intensity measured along the line-of-sight (LOS), as shown in Fig. 2, with the N concentration. The width of the N II emission along the line-of-sight is estimated to be ≈ 5 cm, based on the assumption that the emission originates within the near SOL of width $\lambda_{\mathrm{int}} \approx 1$ cm with a flux expansion factor of ≈ 3, and extends $1-2$ cm into the private flux region. Langmuir probe measurements at the outer target of $3.5-4.5\times10^{19}$ m^{-3} (see Fig. 3) are used to estimate the electron density associated with the emission region. This estimation is consistent with N II line ratio measurements. The derived c_{N} is represented by dashed lines in Fig. 2d, indicating peak values between $\approx 25-40$ %, with shaded regions illustrating the error due to a 20 % uncertainty in electron density.

2.1. Divertor evolution

The detachment qualifier is generalised for this analysis by dividing Eq. 1 by the power fraction directed to the outer divertor on AUG, $f_{\mathrm{div}} = 0.42$, which is derived from assuming two thirds of the power directed to the outer

divertor $f_{\mathrm{div}} = 0.66$ and a fraction $f_{\mathrm{wall}} = 1 - 1/e$ lost to the wall [7, 12]. The f_{div} fraction for MAST-U varies as a function of the distance between primary and secondary separatrices, dr_{sep}. In near connected double-null (i.e. $-1 < dr_{\mathrm{sep}} < 1$ mm), $f_{\mathrm{div}} \approx 0.45$ and, therefore, applying f_{wall} as above, gives $f_{\mathrm{div}} \approx 0.3$.

An overview of the relevant divertor time traces is shown in Fig. 3 for the fuelling and seeding scenarios presented in Figs. 1 and 2, using equivalent colours for consistency. The calculated detachment qualifier is presented first, with vertical dashed lines indicating the points at which $q_{\mathrm{det}} = 1$. The calculation assumes no intrinsic (i.e. carbon) impurity radiation, which is consistent with recent high-fidelity modelling MAST-U [13], though this remains an uncertainty in the analysis.

To determine the point at which partial detachment occurs on MAST-U, data from both the Infra-Red (IR) diagnostic [14] and the Langmuir probes [15] are shown in Fig. 3. The normalised poloidal flux surface ψ_{N} corresponding to the peak heat load measured by IR indicates when the peak first moves away from the target into the SOL. This peak location is also sensitive to the divertor magnetic geometry and, therefore, the interpretation of the peak movement is assessed relative to the attached reference point. In both fuelling and seeding scenarios, there is a clear increase in ψ_{N} coinciding with $q_{\mathrm{det}} \approx 1$.

Next, the electron temperature at the target, $T_{\mathrm{e,LP}}$, determined by the probe located closest to $\psi_{\mathrm{N}} = 1.005$, is shown. High-frequency ELMs make the interpretation challenging, so smoothing is applied for clarity and indicates a drop in $T_{\mathrm{e,LP}}$ to ≈ 5 eV as q_{det} approaches unity. The next panels show the peak electron density measured across the entire target, $n_{\mathrm{e,LP}}$. A roll-over in electron density is typically associated with detachment due to the loss in momentum along the flux surface and strong electron-ion recombination near the target and is observed clearly for the seeding scenarios. The roll-over is less pronounced for the fuelling scenarios, likely due to the injected gas flux being of similar magnitude to the target recycling flux.

To complement the time traces discussed above, poloidal inversions of the total emissivity measured by the infrared video bolometer (IRVB) diagnostic [16, 17] are shown in Fig. 4. The panels show one time slice before partial detachment (Figs. 4a and c) and one time slice after partial detachment occurs (Figs. 4b and d) for the fuelling and seeding scenarios, respectively. Before partial detachment occurs, the emission is strongly localised to both the inner and outer divertors. After partial detachment of the outer divertor occurs, the emission is no longer localised at the inner divertor, and the emission around the outer divertor is spread upstream

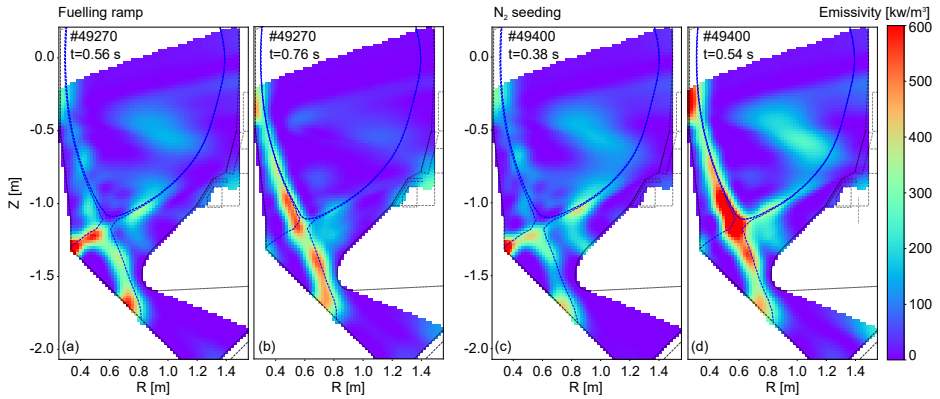

Figure 4: Poloidal inversions of the total emissivity measured by the infrared video bolometer on MAST-U for both the fuelling and seeding scenarios.

Parameter	**AUG**	**JET**	**MAST-U**
$P_{\mathrm{sep}}/R_{\mathrm{maj}}$ MWm^{-1}	$3-10$	$3-7$	$2.5-3$
λ_{q} mm	≈ 2	≈ 2.5	≈ 7
p_0 Pa	$0.8-2.5$	≈ 1.5	$0.3-1.5$
c_{N} %	< 20	< 20	< 25
c_{Ne} %	< 1	< 5	$-$
c_{Ar} %	< 1	< 2	$-$

Table 1: Parameter ranges over which the detachment qualifier has been tested. Impurity concentrations are derived from spectroscopic measurements viewing the outer divertor.

from the target to the X-point. However, since there is still a non-negligible amount of radiation observed at the outer target, this likely indicates that pronounced detachment has not yet been achieved.

A summary of the parameter ranges over which the detachment qualifier has been tested is given in Table 1. While a wide range has been tested in each parameter, reactor scenarios will push to higher divertor pressures ($10-20$ Pa) and higher $P_{\mathrm{sep}}/R_{\mathrm{maj}} > 20$ MWm^{-1}.

3. Divertor reattachment times

The most straight-forward technique to induce a power transient in MAST-U is to vertically shift the plasma from near connected double-null to lower single-null configuration. In this scenario, the power to the outer divertor increases approximately by a factor two in lower single-null (i.e. $dr_{\mathrm{sep}}/\lambda_{\mathrm{q}} > -1$) while the inner target increases by roughly a factor three

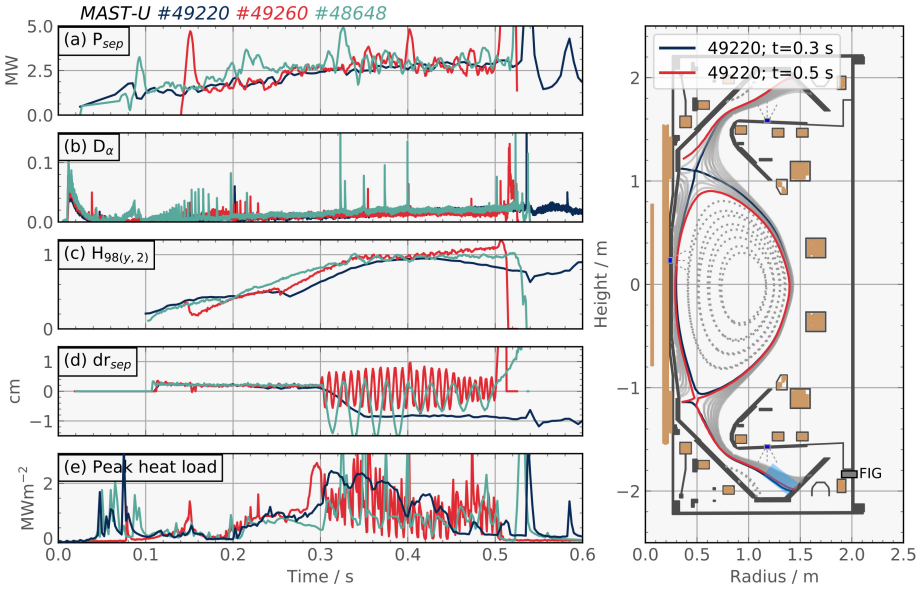

Figure 5: Lower single-null (#49220) and dynamic double-null (#49260 and #49648) H-mode scenarios on MAST-U.

[18]. Since there are currently only two NBI systems available on MAST-U, and typically both beams are required for high performance scenarios, increasing power by NBI is not feasible. Finally, given the difficulty in detaching the conventional divertor, a super-X divertor configuration was chosen which is typically strongly detached in double-null H-mode MAST-U scenarios. The super-X configuration also benefits from wider diagnostic coverage to diagnose the burn-through.

The plasma time traces and machine geometry are shown in Fig. 5. In all scenarios, the super-X configuration is established by $t = 0.3$ s, with a vertical-horizontal inner-outer geometry and outer target strike-point positioned at $R_{\mathrm{t,outer}} \approx R_{\mathrm{maj}} + a_{\mathrm{min}}$. Three scenarios are shown: #49220 features a near connected double-null scenario with a relatively slow transition to lower single-null (denoted steady-state LSN) occurring between $t = 0.3 - 0.35$, while #49260 and #49648 are double-null scenarios with oscillations in vertical position at frequencies of 120 Hz and 40 Hz, respectively, at varying perturbation amplitudes starting at $t = 0.3$ s (denoted dynamic DN). Overall, oscillation frequencies were tested up to and including 200 Hz. A $dr_{\mathrm{sep}} \approx -1$ cm in steady-state LSN, corresponding to a shift of the vertical plasma centroid position of ≈ -10 cm, was found to be the

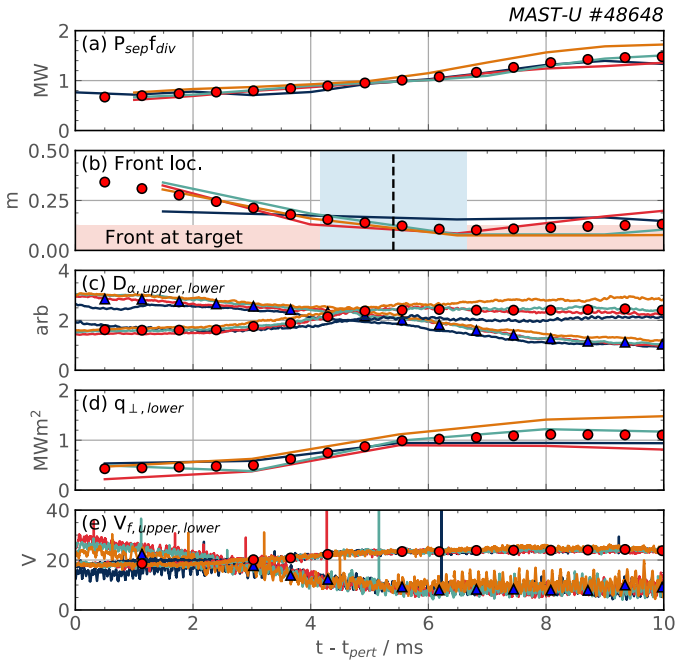

Figure 6: Summary of divertor neutral burn-through measurements. See text for details.

limit before the plasma back transitions into L-mode. Oscillation amplitudes greater than $dr_{\mathrm{sep}} \approx -1$ cm typically triggered large ELMs, as shown by #48648 in Fig. 5.

The steady-state LSN scenario results in an ELM-free H-mode, with $H_{98(\mathrm{y},2)}$ approaching unity and then reducing to ≈ 0.8. Intriguingly, both dynamic DN scenarios have $H_{98(\mathrm{y},2)}$ above one for the full duration of the scenario. However, both dynamic DN scenarios are cut short by disruptions occurring at $t \approx 0.52$ s. The peak heat loads measured at the lower outer divertor by IR show an increase up to ≈ 2 MWm^{-2} during the transition to steady-state LSN, and oscillate between noise levels and ≈ 2 MWm^{-2} during the dynamic DN. In all scenarios, the average peak heat load is decreasing from $t > 0.35$ s, likely due to the rising divertor pressure.

3.1. Divertor evolution

The divertor evolution for the four oscillations during #48648 between $t = 0.4 - 0.5$ s are shown in Fig. 6, with the time axis normalised to the beginning of the downward oscillation in each case. In each panel, red symbols indicate the lower outer divertor values averaged over all oscillations,

while blue symbols, if present, represent the equivalent values in the upper outer divertor. The top panel illustrates the evolution of the power directly driven to the outer target, calculated using a parameterised form of power sharing as a function of dr_{sep} to match results from SOLPS-ITER modelling (see Fig. 3 of [19]). Next, the location of the lower outer divertor deuterium Fulcher band emission, measured by the multi-wavelength imaging (MWI) diagnostic [20], is shown, expressed as the distance from the emission front edge to the target along the divertor leg. The vertical dashed line marks the time when the front reaches the target. An offset of the target location from zero is due to discrepancies between the expected target location from magnetics and the MWI measurement. The blue shaded region indicates the uncertainty, which is determined by the diagnostic time resolution. In the case shown, the derived time for burn-through is $t^{\mathrm{B-T}} = 5.4 \pm 1.25$ ms.

The next panels in Fig. 6 further demonstrate the divertor evolution during the oscillations. Firstly, the divertor D_α emission shows that, before the oscillation begins (i.e. in double-null), the upper divertor D_α is brighter than the lower divertor, with the balance in emission inverting as the plasma moves into lower single-null. The peak heat loads from IR measurements in the lower divertor begin at noise level and then increase up to ≈ 1 MWm^{-2}. Finally, the floating potential, V_{f} measured by the probes, which partly depends on the electron temperature, shows a weak rise in the lower divertor and a more pronounced drop in the upper divertor.

To calculate the predicted burn-through time using Eq. 2, the relevant parameters are determined to be $t^{\mathrm{max}} = 10$ ms, $\Delta P = 0.6$ MW (derived from Fig. 5a), $p_0 = 0.4$ Pa, $n_{\mathrm{e}} = 5 \times 10^{19}$ m^{-3}, $L_{\mathrm{X}} \approx 4$ m (estimated from $R \approx 1$ m), and $V = 2\pi R A_{\mathrm{pol}} \approx 0.4$ m equivalent to the blue shaded region shown in Fig. 5, where $A_{\mathrm{pol}} \approx 0.05$ m^{-2} and $R \approx 1.3$ m. Using these parameters gives a predicted time of $t^{\mathrm{B-T}} \approx 4.3$ ms, within the uncertainty of the measurement. The measured peak heat load in the lower outer divertor does not show any significant change until ≈ 3.3 ms, just prior to the front reaching the target. Conversely, the D_α and V_{f} in the upper divertor are changing after ≈ 1 ms.

A delay in the global response of the divertor can be caused by dynamics of the applied power perturbation. A sinusoidal perturbation waveform, as used in the dynamic DN scenarios, introduces a natural dwell time not accounted for in Eq. 2 due to assuming a linearly increasing power transient. For example, in the scenario shown with a 40 Hz sine wave perturbation, the power distribution changes by $< 2\%$ over 1 ms at the beginning of the transient, compared to $\approx 10\%$ for an equivalent linear perturbation. These dynamics likely explain the relatively short dwell time of ≈ 1 ms observed

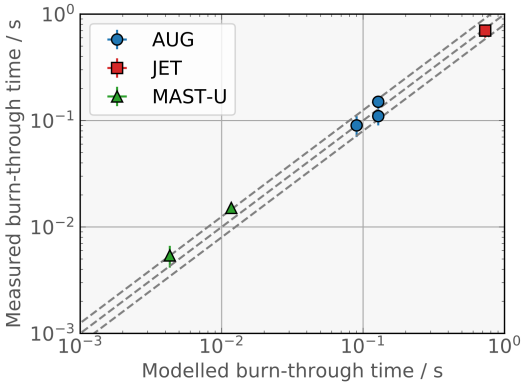

Figure 7: Multi-machine comparison of modelled and measured detachment front burn-through times.

in the upper divertor traces. The relatively longer dwell time of the peak heat load in the lower divertor is consistent with observations on AUG. These demonstrated that, for the same power perturbation induced by a step increase in NBI power, a scenario with a partially detached outer divertor exhibited an almost instaneous rise in divertor temperature, whereas a strongly detached X-point radiator scenario had a dwell time of ≈ 100 ms before the divertor temperature started to increase [8].

In the steady-state LSN scenario, there is a linear change in the plasma vertical position over 50 ms. Burn-through in this scenario occurs within $t^{\mathrm{B-T}} \approx 15 \pm 1.25$ ms, while the model predicts a value of $t^{\mathrm{B-T}} \approx 12$ ms. Similar to the case shown in Fig. 5, the peak heat loads start to rise ≈ 9 ms after the transient, just before the front reaches the target.

Real-time tracking and control of emission fronts in current machines can and do account for delays [21], but these are typically only accounting for delays caused by, for example, gas flow dynamics or the dynamics of the perturbation as discussed above. A delay caused by the front burn-through informs how quickly a control system must influence the divertor plasma (i.e., after incorporating system delays) before the power transient impacts the target temperature.

Providing an absolute uncertainty for the modelled burn-through time is challenging. Factors such as a the volume of neutrals and the power evolution as a function of dr_{sep} are only estimations. The focus should be on using the simplified estimations to understand parameter scaling both across different machines and within a single device. A comparison of burn-through times across AUG, JET and MAST-U is shown in Fig. 7. The pre-

dictions generally align with the measured burn-through times across the three devices, either within the measurement uncertainty or within 25%. Future experiments should evaluate whether the burn-through time significantly changes in scenarios with the same applied power transient and level of detachment, but with detachment induced primarily by impurity seeding and low divertor pressure or by high divertor pressure and low seeding levels. This would test whether the divertor pressure can influence the burn-through time.

4. Conclusions

The simple detachment qualifier developed on AUG has now been tested in three different machines: AUG, JET, and MAST-U. Future experiments should focus on validating the detachment qualifier in extended leg geometries and examining the impact of the toroidal field. Across these devices, the observed time taken to burn-through the neutrals in strongly detached conditions is predicted using the static relation in Eq. 2

To further test the model for predicting the burn-through time, power transients should be conducted in a single device at different divertor pressures and electron densities by adjusting the fuelling and injected power to alter the upstream plasma pressure. Machines capable of alternative divertor configurations, such as MAST-U or TCV, should also test burn-through times with the front located at different distances from the target, primarily varying the volume of the neutrals.

In summary, while further testing is still necessary, it is nonetheless surprising that such simplified models match the different devices with parameters spanning orders of magnitude difference.

Acknowledgements

This work has been carried out within the framework of the EUROfusion Consortium, funded by the European Union via the Euratom Research and Training Programme (Grant Agreement No 101052200 - EUROfusion) and from the EPSRC [grant number EP/W006839/1]. The Swiss contribution to this work has been funded by the Swiss State Secretariat for Education, Research and Innovation (SERI). To obtain further information on the data and models underlying this paper please contact PublicationsManager@ukaea.uk. Views and opinions expressed are however those of the author(s) only and do not necessarily reflect those of the European Union,

the European Commission or SERI. Neither the European Union nor the European Commission nor SERI can be held responsible for them.

References

[1] N. Asakura *et al.*, Nucl. Mater. Ener. **35**, 101446 (2023).

[2] M. Siccinio *et al.*, Plasma Phys. Control. Fusion **58**, 125011 (2016).

[3] R. Wenninger *et al.*, Nucl. Fusion **57**, 046002 (2017).

[4] S. Wiesen *et al.*, Nucl. Fusion **57**, 076020 (2017).

[5] M. Siccinio *et al.*, Fusion Eng. Design. **156**, 111603 (2020).

[6] A. Kallenbach *et al.*, Nucl. Fusion **55**, 053026 (2015).

[7] A. Kallenbach *et al.*, Plasma Phys. Control. Fusion **58**, 045013 (2016).

[8] S. S. Henderson *et al.*, Nucl. Fusion **63**, 086024 (2023).

[9] S. S. Henderson *et al.*, Nucl. Fusion **64**, 066006 (2024).

[10] A. Thornton *et al.*, IAEA FEC 2023, London (2023).

[11] S. S. Henderson *et al.*, Nucl. Fusion **58**, 016047 (2017).

[12] S. S. Henderson *et al.*, Nucl. Mater. Ener. **28**, 101000 (2021).

[13] D. Moulton *et al.*, Nucl. Fusion **64**, 076049 (2024).

[14] J. M. Stobbs, Rev. Sci. Instrum. in review (2024).

[15] P. J. Ryan *et al.*, Rev. Sci. Instrum. **94**, 103501 (2023).

[16] F. Federici *et al.*, Rev. Sci. Instrum. **94**, 033502 (2023).

[17] F. Federici *et al.*, Nucl. Mater. Ener. **submitted**, (2024).

[18] G. D. Temmerman, A. Kirk, E. Nardon, and P. Tamain, J. Nucl. Mater. **415**, S383 (2011).

[19] R. T. Osawa *et al.*, Nucl. Fusion **63**, 076032 (2023).

[20] T. A. Wijkamp *et al.*, Nucl. Fusion **63**, 056003 (2023).

[21] T. Ravensbergen *et al.*, Nat. Commun. **12**, 1105 (2021).